Causal-based optimization of micro-perforated treatments

Cedric Maury[1]
Ecole Centrale Marseille
Laboratory of Mechanics and Acoustics (LMA)
4 impasse Nikola Tesla
13013 Marseille
France

Teresa Bravo[2]
Consejo Superior de Investigaciones Cientificas (CSIC)
Serrano 144
28006 Madrid
Spain

ABSTRACT

Enhancing the low-frequency performance of compact acoustical micro-perforated treatments is a challenging task that requires global optimization studies performed on numerical or theoretical models. However, for a given geometry, there always exists a lower frequency bound below which the treatment will exhibit poor dissipation performance. In this study, it is shown how this lower frequency bound is related to the total integrated dissipated power through a causal-based criterion. Examples are shown for the cases of a rigidly-backed micro-perforate under plane wave incidence and for a locally-reacting micro-perforated resonant silencer mounted in a duct. Such criterion provides the ultimate bandwidth-to-length ratio that can be achieved by the acoustical treatments for a given target dissipation value. One can also deduce the optimal values of individual parameters such as the hole diameters or the wall porosity that leads to a suitable balance between leakage and dissipation effects. The causal-based optimized treatments are validated against simulated or measured impedance tube data.

1. INTRODUCTION

Enhancing the sound absorption properties of micro-perforated treatments is a challenging task if one aims to achieve broadband performance, especially towards the low-frequency range. Moreover, constraints due to ease of integration or fabrication impose to design compact lightweight devices that add further difficulties to achieve low-frequency performance. This is encountered in building acoustics when designing rigidly-backed micro-perforated resonators [1, 2] or transparent space micro-perforated absorbers [3] to lower the room reverberation time over specific low to mid frequency bands without requiring bulky treatments. Micro-perforated panels (MPP) are also suitable to add a controllable amount of resistance and reactance in flow duct wall-treatments in order to

---

[1] cedric.maury@centrale-marseille.fr

[2] teresa.bravo@csic.es

achieve significant noise attenuation over targeted bands without inducing significant pressure losses. This concerns the design of mufflers for automotive silencers [4], of aeronautical liners to reduce the low-frequency components of the noise induced by Ultra-High Bypass Ratio turbofans [5, 6] or the coating of fan casings by MPP resonant absorbers to reduce at source the noise radiated by ventilating and air-conditioning systems [7]. Hence, the optimal design of MPP sound absorbing or attenuating devices in the building and transportation sectors often faces conflicting constraints such as to achieve compactness and high absorption performance over a broad bandwidth, extending towards the low-frequency range [8].

This challenge has been tackled through different strategies. Enlarging the absorption bandwidth can be achieved from a parallel distribution of MPP resonance absorbers [9] with a suitable placement of the individual cell first- and multiple-order resonances [8, 10] to avoid dips between the absorption peaks. Alternatively, this can be realized from the use of ultra-MPPs [11] or purely resistive micro-capillary plates [12] with micrometric hole diameters and calibrated transfer impedance. Extending the absorption performance towards low-frequencies while satisfying space-saving constraints has been addressed used coiled intricate cavities [8, 10] or long extended necks [5] behind the MPPs. The performance can be enhanced by a proper constrained optimisation of the MPP parameters and/or topological optimization of the cavity geometries behind the MPPs with limitations due to additive manufacturing processes that may hinder the absorber acoustic properties [13]. However, whatever the chosen strategy and depending on the practical application, a trade-off has to be found between the maximum absorption value, the absorption bandwidth and the MPP-absorber overall thickness.

In Section 2 of this study, it is examined how a causal-based optimization criterion can be used to find out the optimal MPP parameters that provide maximum wideband performance of rigidly-backed micro-perforated absorbers (MPA) with given thickness while reaching perfect absorption at the Helmholtz resonance frequency. This criterion also determines the ultimate bandwidth-to-thickness ratio that can be achieved by the MPA and, as a consequence, the cut-off frequency below which the MPA will exhibit poor absorption performance. It is extended in Section 3 to the case of a MPP-coated meta-silencer with Acoustic Black Holes (ABH) functionality, e.g. able to reduce both noise transmission and reflection. Section 4 shows causal-based optimization of one or two MPP parameters of a MPP-ABH silencer. Section 5 provides concluding remarks and perspectives.

2. CAUSAL-BASED OPTIMISATION OF RIGIDLY-BACKED MPAs

Causal relationships are presented that relate the optimal absorption bandwidth and total thickness of a rigidly-backed MPA under normal incidence.

2.1. Causal relationship
One considers a rigidly-backed MPA, as shown in Fig. 1, made up of a MPP with circular holes of diameter d, thickness t and separation distance Λ, rigidly-backed by a cavity of depth D, onto which impinges a normally incident plane wave.
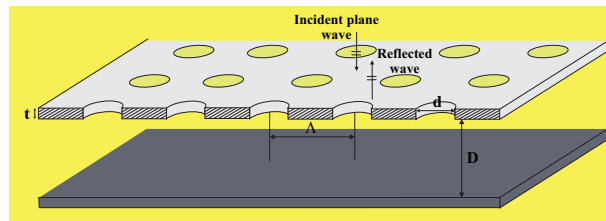

Figure 1. Sketch of a rigidly-backed MPA under normal incidence.

At low frequencies, the MPA effective input impedance can be recast in the form $Z = (\mathrm{j}m/\omega)\left[\omega^2 - \omega_H^2 - \mathrm{i}\omega\xi t/m\right]$ with $m = \rho_0 t k_m/\sigma$ the MPP effective mass, $\omega_H^2 = \rho_0 c_0^2/(mD)$ the MPA Helmholtz resonance frequency and $\xi = 32\eta k_r/(\sigma d^2)$ the MPA damping term, ρ_0 and c_0 being the density and sound speed in air, σ the MPP perforation ratio and η the air dynamic

viscosity. $k_m(\text{Sh},d,t)$ and $k_r(\text{Sh},d,t)$ are inertial and resistive quantities that depend on $\text{Sh} = (d/2)\sqrt{\rho_0\omega/\eta}$ the Shear number, namely the ratio between the holes radius and the in-hole viscous boundary layer thickness. They have been modelled by Maa [1] for submillimetric holes.

A quantity of interest is the complex reflection coefficient $r = (Z - Z_0)(Z + Z_0)^{-1}$ with $Z_0 = \rho_0 c_0$. Because of causality, Titchmarsh theorem [14] implies that $r(f)$ is analytic with no poles in the lower half of the complex frequency plane sketched in Figure 2. One can then define $r'(f) = r(f)\prod_{n=1}^{\infty}(f - f_n^*)(f - f_n)^{-1}$, an analytic function with no poles nor zeros in the lower half-plane of complex f, such that $r(f_n) = 0$. From Cauchy's theorem, one has $\oint_C \log(r'(f))f^{-2}\,df = 0$ where the closed contour C is shown in red in Figure 2.
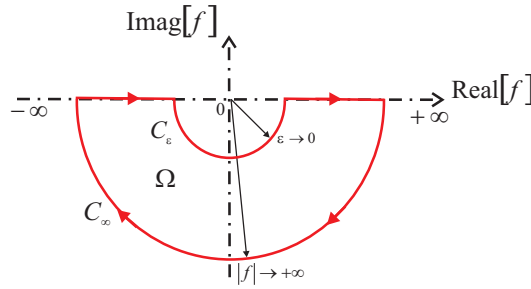

Figure 2. Integration contour of $r'(f)$ in the lower-half complex frequency plane.

Summing up the contribution to the integral of each contour element, one gets

$$2\int_0^{\infty} \log(|r(f)|)\frac{df}{f^2} = -\lim_{\varepsilon \to 0}\text{Real}\left[\int_{C_\varepsilon}\log(r(f))\frac{df}{f^2}\right] + 2\pi\,\text{Im}\sum_{m=1}^{M}\frac{1}{f_m}, \tag{1}$$

where $\{f_m\}_{m=1,\ldots M}$ are the zeros of r comprised within C. Inserting the low-frequency approximation $\log(r(f)) \approx -2i\omega Z_0/(m\omega_H^2)$ into the first right-hand side integral, one obtains

$$\int_0^{\infty} \log(|r(f)|)\frac{df}{f^2} = -\frac{2\pi^2 D}{c_0} + \pi\sum_{m=1}^{M}\text{Imag}\left(\frac{1}{f_m}\right). \tag{2}$$

with $\sum_{m=1}^{M}\text{Imag}(1/f_m) \geq 0$. Solving for $Z(\omega) = Z_0$ provides exact expressions for the zeros of r that read $f_0^{\pm} = -i(Z_0 - \xi t)/(4\pi m) \pm \sqrt{f_H^2 - (Z_0 - \xi t)^2/(4\pi m)^2}$. Therefore, Eq. (2) yields the following causal relationship for a MPA under normal incidence

$$-\frac{c_0}{2\pi^2}\int_0^{\infty}\log(|r(f)|)\frac{df}{f^2} = \begin{cases} D\dfrac{\xi t}{Z_0} & \text{if} \quad \xi t < Z_0 \\ D & \text{otherwise} \end{cases}. \tag{3}$$

Assuming a target absorption $\alpha_0 = 1 - |r_0|^2$ over a specific bandwidth $[f_{\min}, f_{\max}]$, Eq. (3) provides an ultimate bandwidth-to-thickness ratio $\Delta\lambda/D$ that can be achieved by the MPA, namely

$\Delta\lambda/D \leq 4\pi^2 \big/ \big\| \log(|1-\alpha_0|) \big\|$ with $\Delta\lambda = c_0\left(f_{\min}^{-1} - f_{\max}^{-1}\right)$. Assuming $f_{\max} \to \infty$ and $\alpha_0 = 0.9$, this implies that, for a given cavity depth D, a wideband MPA will exhibit poor absorption performance below its cut-off frequency, $f_{c,\min} = c_0/(17D)$.

2.2. Causal optimisation of rigidly-backed MPAs

One considers a rigidly-backed MPA with cavity depth $D = 0.04\,\mathrm{m}$. Figure 3 shows the individual effect of the MPP parameter on the total intensity reflection coefficient (in logarithmic scale) integrated over all wavelengths, namely $T_r(d,\Lambda,t) = -\left(c_0/2\pi^2\right)\int_0^\infty \log(|r(f)|)f^{-2}\mathrm{d}f$ in frequency variables, that corresponds to the left-hand side of the causal relationship given by Eq. (3). The integral is evaluated from Gauss-Legendre quadrature over 20000 points distributed between 0.1 Hz and 20 kHz. It exactly coincides in Figs. 3(a), (c) and (e) with the analytical function on the right-hand side of Eq. (3), with slope discontinuity for the MPP parameter observed when t, d or Λ satisfy $\xi t = Z_0$.

For each row figures, two out of the three MPP parameters are fixed amongst $d_0 = 0.5\,\mathrm{mm}$, $t_0 = 1\,\mathrm{mm}$ and $\Lambda_0 = 5\,\mathrm{mm}$, letting d, t and Λ vary in Figs 3(a-b), 3(c-d) and 3(e-f), respectively. In either case, an optimal value of the variable parameter is observed that provides perfect absorption at the MPA Helmholtz resonance. For instance, varying the MPP holes diameter d while keeping fixed parameters for the MPP thickness ($t_0 = 1\,\mathrm{mm}$) and for the holes pitch ($\Lambda_0 = 5\,\mathrm{mm}$), an optimal value, $d_{\mathrm{opt}} = 0.48\,\mathrm{mm}$, is found from Figs. 3(a) and (b) at which perfect absorption is achieved, e.g. $\alpha_{\max}(\omega_H) = 1$ at 546 Hz. When d falls below d_{opt}, the integrated reflection coefficient stays constant equal to D, in accordance with Eq. (3). As shown in Fig. 3(b) [green curve], the absorption half-bandwidth then broadens while the absorption peak value drops by an amount such that the total integrated reflection coefficient stays constant. When d increases above d_{opt}, both the absorption half-bandwidth and peak value decrease, as seen from the grey curve in Fig. 3(b).
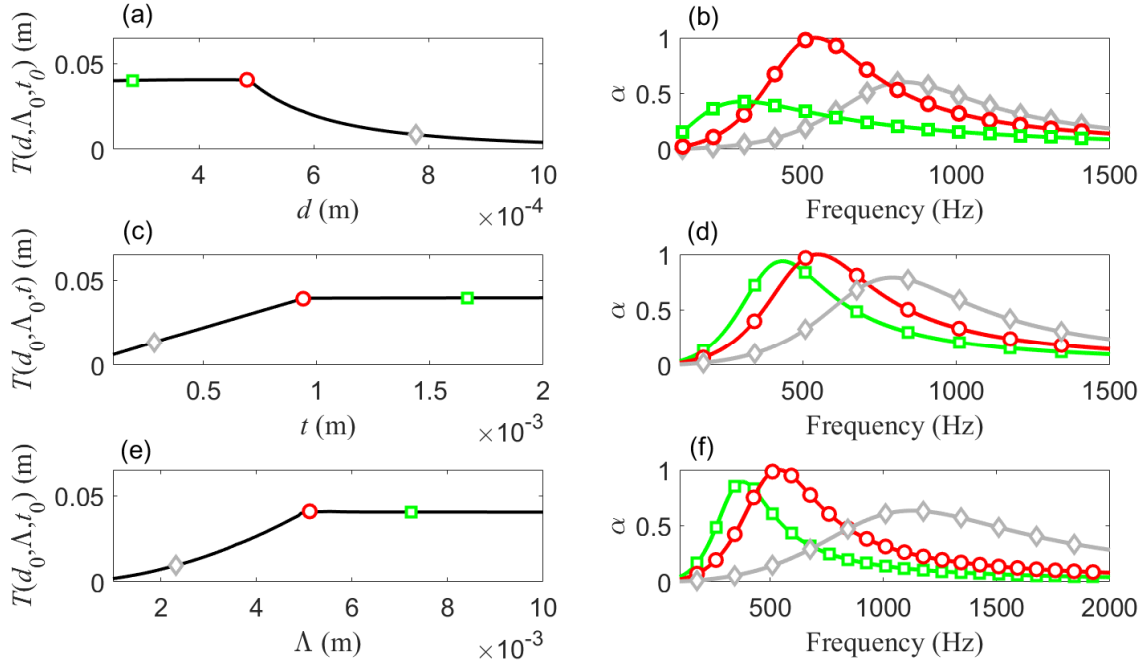

Figure 3: Influence of the holes diameter (a), panel thickness (c) and holes pitch (e) parameters on the total power dissipated by a rigidly-backed MPP absorber; the corresponding absorption spectra are shown in (b), (d) and (f) for over-damped (green), critically-coupled (red) and under-damped (grey) configurations.

Varying t in Figs. 3(c-d) while keeping d_0 and Λ_0 fixed leads to an optimal MPP thickness $t_{opt} = 0.94$ mm at which the losses balance the leakage, thereby providing perfect absorption at 544 Hz. Similarly, varying Λ in Figs. 3(e-f) while keeping t_0 and d_0 fixed leads to an optimal MPP holes pitch $\Lambda_{opt} = 5.1$ mm at which the MPA is critically-coupled, yielding unit absorption at 512 Hz. In each case, a critical value, t_{opt} (resp. Λ_{opt}) exists above which the loss-to-leakage factor, $C_d/C_l = \xi t/Z_0$, increases but without changing the MPA overall thickness required to achieve the corresponding total absorption performance [grey curves in Figs. 3(d) and (f)].

2.3. Causally-guided MPA design: experimental validation

The optimal MPP parameters obtained from Figs. 3(a), (c) and (e) maximize the sensitivity of the total intensity reflection with respect to the corresponding MPP parameters. For instance, $\Lambda_{opt} = 5.1$ mm in Fig. 3(e) satisfies $\Lambda_{opt}(d_0, t_0) = \arg \max_\Lambda |dT_r/d\Lambda|$ [15]. More generally, letting t and d vary, an optimal design surface can be obtained that shows the locus of points $\Lambda_{opt}(t,d)$ that maximize $|\partial T_r/\partial \Lambda|$ for each pair (t,d). It is shown in Fig. 4(a) and can be compared, for validation, to the optimal design surface shown in Fig. 4(b) that satisfies the critical coupling condition $\xi t = Z_0$ in Λ. All the points on these causal optimal surfaces are associated to MPP parameter $(t_{opt}, d_{opt}, \Lambda_{opt})$ that ensure unit absorption at the MPA Helmholtz resonance.
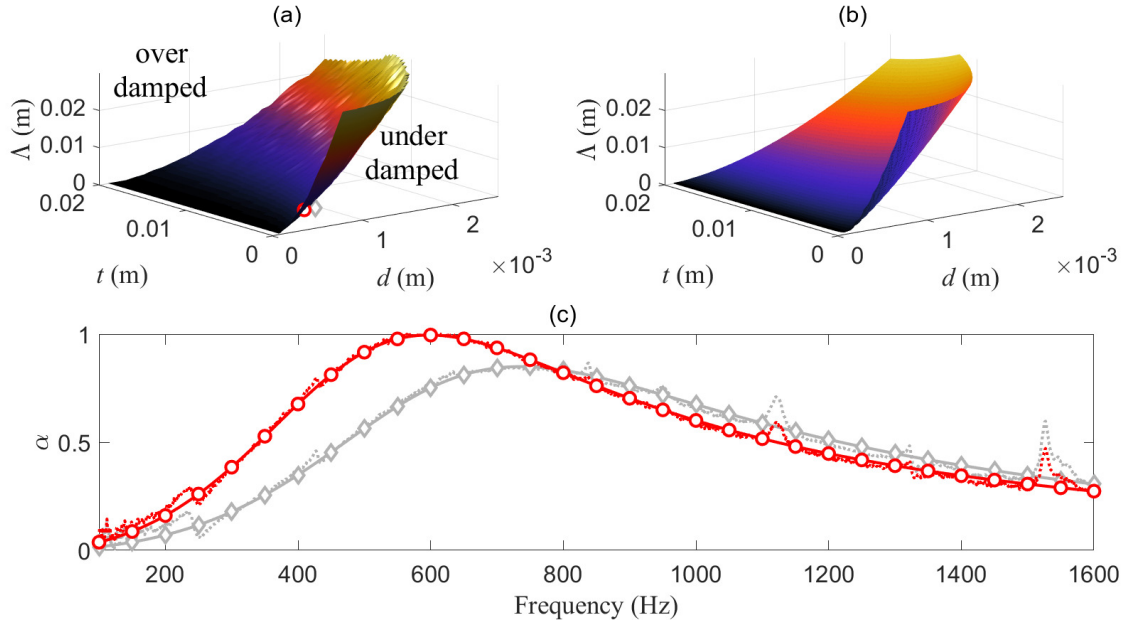

Figure 4: Locus of the optimal MPP parameters in the design space (t,d,Λ): (a) when maximizing $|\partial T/\partial \Lambda|$ or (b) from the critical coupling condition $\xi t = Z_0$; (c) Absorption spectra corresponding to the nominal (grey diamond) and optimal (red circle) MPP parameters whose design space location is shown in (a): theoretical calculation (plain) and Kundt tube measurements (dotted).

Figure 4(c) shows the simulated absorption of two MPAs with cavity depth $D = 0.06$ m, MPPs thickness $t_0 = 0.5$ mm and holes pitch $\Lambda_0 = 5$ mm, but with holes diameter reduced from $d_0 = 0.5$ mm in the nominal case (grey diamond) down to $d_{opt} = 0.42$ mm in the causal-based optimal configuration (red circle). The corresponding change of parameters in the design space is shown in Fig. 4(a). The acoustical performance of the nominal and optimized MPPs have been experimentally verified in a Kundt tube using the two-microphones method under plane wave normal incidence method up to the duct cut-on frequency of 2.1 kHz [16]. The MPPs have been manufactured

from mechanical machining. Figure 4(c) shows a good correlation between the impedance-based analytical simulations and those measured as for the nominal and optimal configurations, apart from localized absorption peaks due to the MPP volumetric resonances. In the optimal case, one observes a broadband absorption with unit peak value at the MPA Helmholtz resonance frequency around 600 Hz. The simulations and measurements shown in Figs. 3 and 4 correspond to the causal cut-off frequencies, $f_{c,\min} = 500\,\text{Hz}$ and $f_{c,\min} = 340\,\text{Hz}$ respectively, below which the MPA cannot exhibit high absorption performance.

3. CAUSAL-BASED OPTIMISATION OF MPP-COATED ABH SILENCERS

The causal relationships derived in Section 2 for rigidly-backed MPAs under normal incidence are now extended to the case of MPP-coated locally-reacting duct wall-treatments able to reduce both transmission and reflection, e.g. to emulate an ABH effect. A basic type of ABH silencers of length L is made of a serial distribution of N cavities of width d_c separated by rigid walls of thickness d_w whose depth $D_n\,(n=1\ldots N)$ follows a power-law variation along the duct of radius R, as the one sketched in Figure 5. The cavity-duct interface may be coated with MPP treatment to limit the occurrence of flow-induced noise. The current study will only focus in the no-flow case.
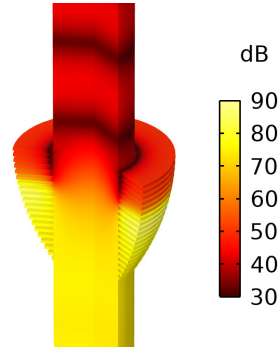

Figure 5: ABH silencer made up of 20 annular cavities whose depths follow a square-law variation; finite element simulation of the sound pressure levels induced by an incident plane wave propagating upward at 1.4 kHz.

3.1. Causal relationship

Unlike the rigidly-backed MPA where the dissipated power η was the absorption $\alpha = 1 - |r|^2$, the power dissipated by the ABH silencer is either absorbed or transmitted, so that $1 - \eta = |r|^2 + |t|^2$ with t the silencer transmission coefficient. A quantity of interest in the causal approach is the total dissipated power $T_\eta = -\left(c_0/4\pi^2\right)^{-1}\left[\int_0^\infty \log[1 - \eta(f)]f^{-2}\mathrm{d}f\right]$. Since $1 - \eta \geq |t|^2$, an upper bound for the total transmitted power $T_t = -\left(c_0/4\pi^2\right)^{-1}\left[\int_0^\infty \log\left(|t(f)|^2\right)f^{-2}\mathrm{d}f\right]$ will also be an upper bound for T_η.

Because of causality, $t(f)$ is analytic in the lower half-plane of complex f (see Fig. 2) with no poles, but possible zeros denoted f_m in this domain. An integral relationship, similar to Eq. (2), is also obtained for the transmission coefficient

$$\int_0^{+\infty} \log\left(|t(f)|\right)^2 \frac{\mathrm{d}f}{f^2} = \pi\,\mathrm{Im}\left[\left.\frac{dt}{df}\right|_{f=0}\right] + 2\pi\,\mathrm{Im}\sum_{m=1}^M \frac{1}{f_m}, \tag{4}$$

with $\sum_{m=1}^{M} \text{Im}(1/f_m) \geq 0$, so that $T_\eta \leq (c_0/4\pi)\text{Im}[dt/df|_{f=0}]$. A transfer matrix method (TMM) is used to provide a first-order Taylor series expansion of $t(f)$ around $f=0$ and to assess the effect of MPP coating on this upper bound. It leads to:

$$t(f) = 1 - j\pi f \left[\frac{SM}{Z_0} + \frac{Z_0 C}{S} \right] + \vartheta(f^2), \tag{5}$$

with $S = \pi R^2$, $M = Z_0 L/(S c_0)$, $C = SL/(Z_0 c_0) + S_{cav}(\sigma Z_0 c_0)^{-1} \sum_{n=1}^{N}(D_n + D_n^2/2R)$ and $S_{cav} = 2\pi Rd$.

The influence of MPP appears through the wall porosity that reads $\sigma = d_c/(d_c + d_w)$ without MPP and $\sigma = \pi d^2/(4\Lambda^2)$ with MPP coating, but also in higher-order terms in the series expansion. A cut-off frequency $f_{c,min}^{ABH}$ can also be deduced from Eq. (5) below which a wideband ABH silencer will exhibit poor dissipation performance. It reads

$$f_{c,min}^{ABH} = \frac{c_0 |\log(1-\eta_0)|}{\pi^2 L \left[2 + \dfrac{V_{ABH}}{\sigma V_D} \right]}, \tag{6}$$

with V_{ABH} the volume occupied by the ABH cavities and $V_D = SL$ the volume occupied by the lined duct section. Equation (6) yields several strategies in order to decrease $f_{c,min}^{ABH}$. This can be achieved either by increasing the ABH overall length L, often constrained, or the relative volume V_{ABH}/V_D between the silencer and the duct section, also limited, or by decreasing the wall porosity σ, which can be achieved by micro-perforating the ABH-duct interface. This would also bring the aerodynamic benefit to reduce flow-induced noise.

3.2. Causal optimisation of MPP-coated ABH silencers

One considers an ABH silencer of length $L = 0.1\,\text{m}$ made up of a serial distribution of $N = 15$ cavities of width $d_c = 4.7\,\text{mm}$ whose depths $D_n (n=1...N)$ follow a power-law variation up to $D_{max} = 47\,\text{mm}$ along a duct of radius $R = 47\,\text{mm}$. First, an optimal cavity wall thickness of $d_{w,opt} = 2\,\text{mm}$ was found from the causal-based criterion, $d_{w,opt} = \arg\max_{d_w} |\partial T_\eta/\partial d_w|$, e.g. from maximizing the sensitivity of the total integrated power dissipated by the ABH with respect to d_w. It leads to the blue dissipation curve seen in Fig. 6(b) for which almost perfect dissipation is observed above 1.4 kHz up to the duct cut-on frequency, associated with minute reflected and transmitted powers over this wideband ABH efficiency range. Second, one assumes that the ABH cavities are coated by a cylindrical MPP. Two out of the three MPP parameters are fixed amongst $d_0 = 1\,\text{mm}$, $t_0 = 0.5\,\text{mm}$ and $\Lambda_0 = 5\,\text{mm}$, letting d, t and Λ vary individually in Figs 6, 7 and 8, respectively.

It can be seen from Fig. 6 that an optimal value of the MPP holes diameter is found, $d_{opt} = 1.34\,\text{mm}$ [red circle in Fig. 6(a)], for which the total amount of energy entering the MPP-coated ABH silencer is essentially dissipated by visco-thermal losses through the MPP apertures and within the ABH cavities. It leads to high dissipation values [red curve in Fig. 6(b)] that stay greater than 0.95 between 960 Hz and 1.4 kHz. When d is greater than d_{opt}, the wall porosity of the silencer increases, thereby reducing the effective mass induced by the MPP holes. As a consequence, it upshifts the resonance frequencies of the ABH cavities coated by the MPP and reduces the ABH efficiency bandwidth [grey curve in Fig. 6(b)] as well as the total integrated dissipated power [grey diamond in

Fig. 6(a)]. When d decreases below d_{opt}, the high-valued dissipation plateau turns into a maximum dissipation hump. Its peak value, observed at 740 Hz in Fig. 6(b) (green curve), decreases while its half-bandwidth broadens, so that the total dissipated power T_η stays constant.
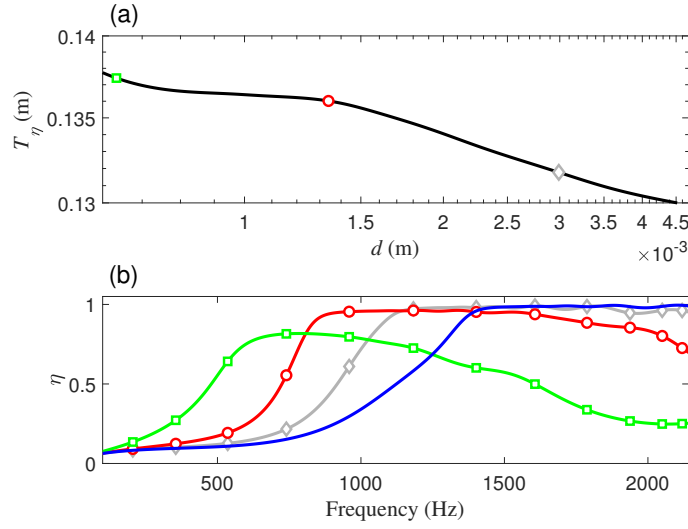

Figure 6: (a) Influence of the MPP holes diameter on the total integrated power dissipated by the ABH silencer calculated by TMM; (b) Power dissipated by the ABH silencer when uncoated (blue) and MPP-coated: $d = 0.64$ mm (green), $d = 1.34$ mm (red) and $d = 3$ mm (grey).

Keeping fixed values $d_0 = 1$ mm and $t_0 = 0.5$ mm for the MPP, it can be seen from Fig. 7 that an optimal value of the MPP holes pitch is found, $\Lambda_{opt} = 4.2$ mm [red circle in Fig. 7(a)] leading to a high amount of dissipation greater than 0.95 between 960 Hz and 1.4 kHz [red curve in Fig. 7(b)]. When Λ is lower than Λ_{opt}, the wall porosity of the silencer increases, thereby upshifting the resonance frequencies of the ABH cavities coated by the MPP and reducing the ABH efficiency bandwidth [grey curve in Fig. 7(b)] as well as the total integrated dissipated power [grey diamond in Fig. 7(a)]. When Λ increases above Λ_{opt}, the high dissipation plateau becomes a broadband dissipation hump whose peak value at 600 Hz reaches 0.76 in Fig. 7(b) (green curve).
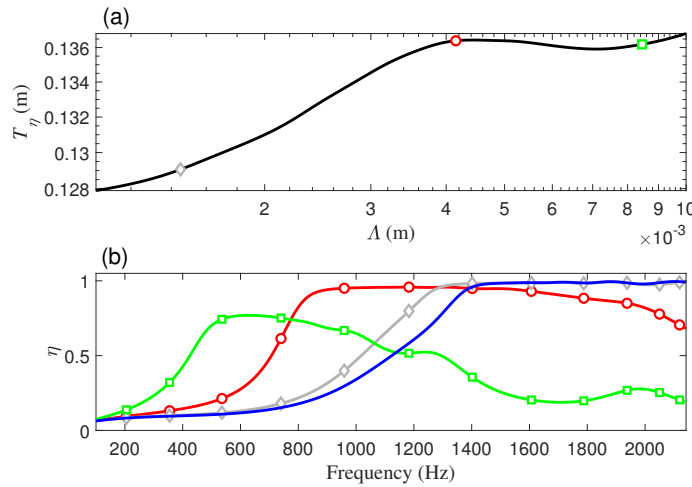

Figure 7: (a) Influence of the MPP holes pitch on the total integrated power dissipated by the ABH silencer calculated by TMM; (b) Power dissipated by the ABH silencer when uncoated (blue) and MPP-coated: $\Lambda = 1.5$ mm (grey), $\Lambda = 4.2$ mm (red) and $\Lambda = 8.4$ mm (green).

The influence of increasing the MPP perforation ratio, for instance by decreasing the holes pitch, onto the dissipation, reflection and transmission power coefficients is shown in Fig. 8. An optimal value of the perforation ratio (or wall porosity) is found, $\sigma_{opt} = 2.9\%$ [red circle in Fig. 8(a)] providing a large amount of dissipation between 960 Hz and 1.4 kHz, as already seen in Fig. 7(b). In the meantime, it is observed in Fig. 8(c) that the reflection coefficient falls below 0.05 above 960 Hz for $\sigma \leq \sigma_{opt}$ while the transmission coefficient does not exceed 0.05 between 960 Hz and 1.4 kHz only if $\sigma = \sigma_{opt}$ tending towards large values when σ is much smaller than σ_{opt}. Indeed, in the latter case, the MPP-coated ABH silencer tends towards a rigid duct section with zero reflection coefficient and full transmission. On the opposite, if σ is much greater than σ_{opt}, the MPP-coated ABH silencer tends towards an uncoated ABH silencer and the performance shown by the grey curves in Figs. 6 to 8 tend towards the limiting "blue curve" performance.
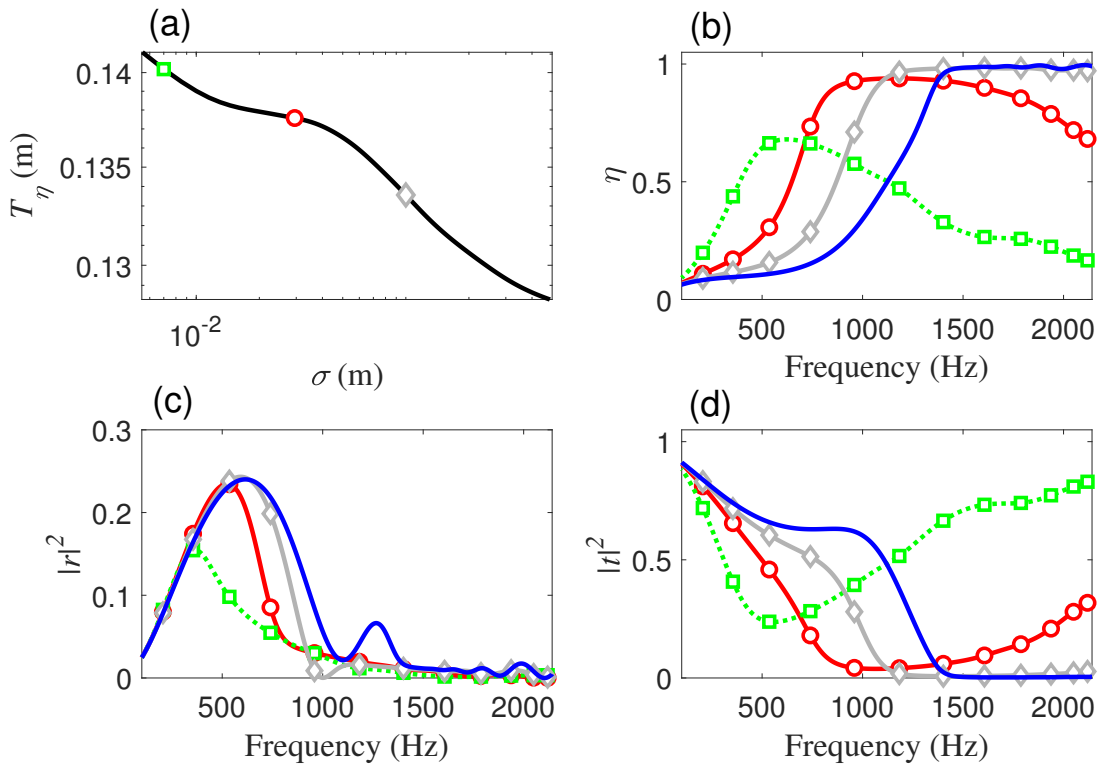

Figure 8: (a) Influence of the MPP perforation ratio on the total integrated power dissipated by the ABH silencer calculated by TMM; Power dissipated (b), reflected (c) and transmitted (d) by the ABH silencer when uncoated (blue) and MPP-coated: $\sigma = 0.7\%$ (green), $\sigma = 2.9\%$ (red) and $\sigma = 10\%$ (grey).

In accordance with Eq. (6), it can be seen that decreasing the wall porosity by decreasing the MPP holes diameter (Fig. 6), by increasing the holes pitch (Fig. 7) or by decreasing the perforation ratio (Fig. 8) contributes to lower the causal-based cut-off frequency below which the MPP-coated ABH silencer will be inefficient.

The optimal and non-optimal dissipation performance of a MPP-coated ABH silencer simulated by the transfer matrix approach are now compared in Fig. 9 against those modelled using Comsol Acoustics finite element software. A good correlation is observed in Fig. 9 confirming the validity for the TMM assumption of pointwise scatterers for the MPP-coated cavities and plane wave propagation in the duct and cavity domains below their cut-off frequencies.
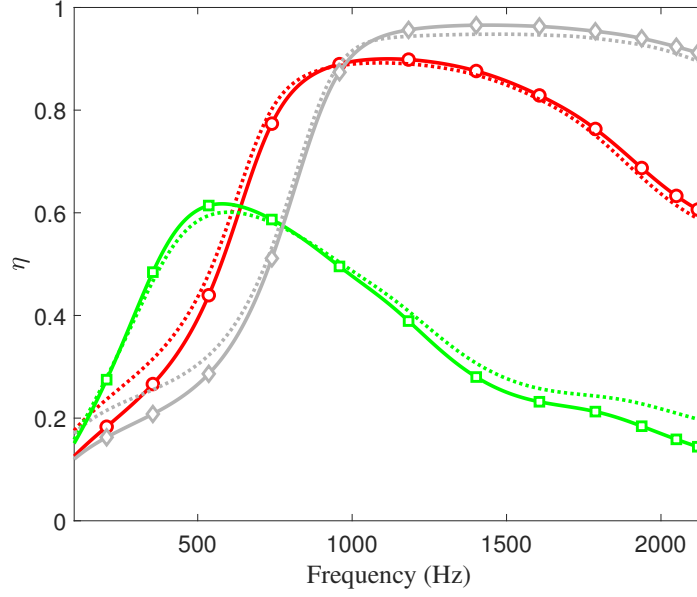
Figure 9: Power dissipated by the MPP-coated ABH silencer modelled from transfer matrix (plain with markers) and finite element (dotted) methods: $\sigma = 0.7\,\%$ (green), $\sigma = 2.9\,\%$ (red) and $\sigma = 10\,\%$ (grey).

Keeping a fixed value $t_0 = 0.5\,\text{mm}$ for the MPP thickness, Fig. 10(a) shows that a two-parameter causal-based optimization can be performed in the (d, Λ) design space. A curve of optimal design parameters $(d_{\text{opt}}, \Lambda_{\text{opt}})$ exists at the edge of the T_η plateau-like surface that maximize the total integrated dissipated power without restricting its efficiency range, as it would be the case if $d \leq d_{\text{opt}}$ and $\Lambda \leq \Lambda_{\text{opt}}$. A number of optimal parameters has been picked up on the optimal edge line that lead in Fig. 10(b) to very similar broadband dissipation curves for MPP-coated ABH silencers with very high performance.
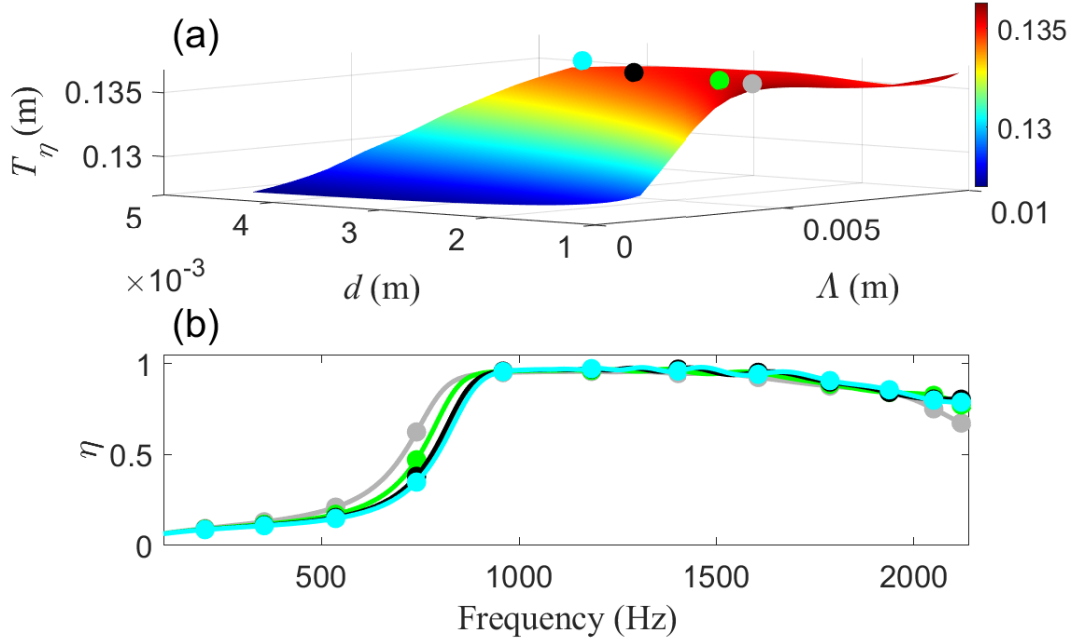

Figure 10: (a) Influence of the MPP holes diameter and pitch on the total integrated power dissipated by the MPP-coated ABH silencer; (b) Power dissipated by the silencer when $(d, \Lambda) = (1.1\,\text{mm}, 4.5\,\text{mm})$ (grey), $(d, \Lambda) = (2.1\,\text{mm}, 6.5\,\text{mm})$ (green), $(d, \Lambda) = (3.6\,\text{mm}, 8.5\,\text{mm})$ (black) and $(d, \Lambda) = (4.6\,\text{mm}, 10\,\text{mm})$ (cyan).

4. CONCLUSIONS AND PERSPECTIVES

This study examined how a causally-guided formulation is able to provide the optimal parameters of MPP coatings either over a rigidly-backed cavity or over an ABH duct silencer. It provides an ultimate bandwidth-to-thickness ratio as well as an optimization criterion based on maximization of the total integrated dissipation that ensures full dissipation on the incident energy at the absorbers Helmholtz-type resonances. Such causally-guided optimal design of MPAs has been verified experimentally for rigidly-backed MPAs and numerically for MPP-coated ABH-type silencers.

It yielded to a cut-off frequency below which the absorber exhibits poor dissipation performance, thereby constituting a lower frequency bound for acoustic optimization studies. It is downshifted by solely increasing the depth of the backing cavity for rigidly-backed MPAs whereas, for the MPP-coated ABH silencers, the situation is more complex. Its efficiency range is extended towards low-frequencies by increasing the ABH overall length or the volume ratio between the silencer and the duct section or by decreasing the wall porosity, e.g. by reducing the MPP holes diameter, by increasing the holes pitch or by decreasing the perforation ratio. Hence, coating ABH silencers with optimized MPPs is a solution to enlarge the efficiency range of ABH silencers towards low-frequencies, both in transmission (to mitigate exhaust noise emissions) and in reflection (to avoid the triggering of thermo-acoustic instabilities in combustion chambers).

In order to overcome the reduction in bandwidth and maximum dissipation due to the added resistance brought by the MPP coatings, a simultaneous optimisation of the MPP and ABH silencer parameters should be performed guided by the causal approach and validated against a metaheuristic global optimization process. It is anticipated that the introduction of MPP coatings would reduce flow-induced noise generation while preserving the ABH performance. However, computational fluid dynamics simulations should be performed to determine the range of flow and MPP parameters able to conciliate these aeroacoustic objectives.

REFERENCES

1. D.Y. Maa, Potential of microperforated panel absorbers, *Journal of the Acoustical Society of America* 104(5): 2861–2866, 1998.
2. H.V. Fuchs and X. Zha, Acrylic-glass Sound Absorbers in the Plenum of the Deutscher Bundestag, *Applied Acoustics* 51(2): 211–217, 1997.
3. K. Sakagami, M. Kusaka, T. Okuzono, S. Kido and D. Yamaguchi. Application of transparent microperforated panels to acrylic partitions for desktop use: A case study by prototyping. *UCL Open: Environment*, 2: 09, 2021.
4. S. Allam and M. Åbom, A new type of muffler based on microperforated tubes, *ASME Journal of Vibration and Acoustics,* 133: 031005, 2011.
5. F. Simon, Long Elastic Open Neck Acoustic Resonator for low frequency absorption, *Journal of Sound and Vibration,* 421: 1–16, 2018.
6. R. Billard, Study of perforated liners for aeronautics, Ph.D. Dissertation in Acoustics, Université du Maine, 2021. https://tel.archives-ouvertes.fr/tel-03247946
7. F. Czwielong, S. Floss, M. Kaltenbacher and S. Becker, Influence of a micro-perforated duct absorber on sound emission and performance of axial fans, *Applied Acoustics,* 174: 107746, 2021.
8. M. Yang, S. Chen, C. Fu and P. Sheng, Optimal sound-absorbing structures, *Material Horizons*, 4: 673–680, 2017.

9. C. Wang and L. Huang, On the acoustic properties of parallel arrangement of multiple micro-perforated panel absorbers with different cavity depths, *Journal of the Acoustical Society of America,* 130: 208–218, 2011.
10. F. Wu, X. Zhang, Z. Ju, J. Zhao, M. Hu, M. Gao, J. Luo and H. Pu, Ultra-Broadband Sound Absorbing Materials Based on Periodic Gradient Impedance Matching, *Frontiers in Materials*, 9: 909666, 2022.
11. Q.-Y. Jie, K. Cui, S.-M. Liu, Z.-B. Li, D.-Y. Kong and S.-M. Sun, Development of Broadband Ultra Micro-Perforated Panels Based on MEMS Technology, *Applied Mechanics and Materials*, 5: 535, 788 – 795, 2014.
12. C. Maury and T. Bravo and C. Maury, Wideband sound absorption and transmission through micro-capillary plates: Modelling and experimental validation, *Journal of Sound and Vibration*, 478: 115356, 2020.
13. J. Kennedy, L. Flanagan, L. Dowling, G. J. Bennett, H. Rice and D. Trimble, The influence of additive manufacturing processes on the performance of a periodic acoustic metamaterial, *International Journal of Polymer Science*, 2019: 7029143, 2019.
14. E. C. Titchmarsh, *Introduction to the theory of Fourier integrals*, 2nd Edition, Oxford Clarendon Press: Oxford, 1937.
15. T. Bravo and C. Maury, Causally-guided acoustic optimization of rigidly-backed micro-perforated partitions: Theory, *Journal of Sound and Vibration*, 520: 116634, 2022.
16. T. Bravo and C. Maury, Causally-guided acoustic optimization of rigidly-backed micro-perforated partitions: Case studies and experiments, *Journal of Sound and Vibration*, 523: 116735, 2022.